UiT
THE ARCTIC
UNIVERSITY
OF NORWAY

Faculty of Science and Technology
Department of Physics and Technology

Geoelectrical structures beneath Spitsbergen-Svalbard derived from magnetotelluric imaging

—

Thomas I. Beka
*A dissertation for the degree of Philosophiae Doctor – April 2016*

UNIVERSITY OF TROMSØ

Abstract

In this thesis a series of geophysical surveys are carried out on the geologically important and remote Svalbard using magnetotelluric imaging, to constrain better the geology particularly defining geothermal resources. Magnetotellurics (MT) relays on natural source time-varying electric and magnetic field data measured at the earth's surface in order to derive the subsurface resistivity structure. As part of the thesis, broadband MT data are collected in central and northwestern Spitsbergen in the period range between 0.003 - 1000 s from nearly 80 stations distributed along five profiles of 6 - 42 km long.

The new MT data have brought significant contributions to extend the existing crustal scale geological knowledge, which mostly inferred from surficial, seismic and gravity studies in the past. From the MT data, we derived 2D and 3D resistivity models for selected areas and enabled to image the structure of the near surface bedrock geology and crustal scale architecture.

The 2D and 3D inversion results indicated reasonable agreement with previous geological data, models and well reflected tectonic histories. Within the Central Tertiary Basin a higher frequency of fractures, localized faults and thick intrusive dyke swarms are resolved in the sub-horizontal and less deformed Mesozoic platform cover deposits. The tectonic history of the Paleocene-Eocene fold-thrust belt structure in northwest Svalbard is well indicated in the MT data from the Brøgger peninsula as a deformed architecture. The MT data from this section imaged elegantly an interplay between repeated basement-involved fold-thrust structures and successive down-dropped strata along steeply dipping oblique-normal faults that created a horst/ridge and graben/depression systems. MT is sensitive to subsurface geothermal attributes, such as fluid and heat migration zones. In this respect, the new MT data have proposed locations that may favour technologically accessible geothermal potentials.

"Everything should be made as simple as possible, but not simpler"

Albert Einstein

Acknowledgements

Contents

Chapter 1

Introduction

1.1 Motivation

In comparison to other energy resources a lesser amount of attention is given to deep geothermal energy exploration and development in Norway and its Arctic territories. In the case of Svalbard, this is partly due to lack of awareness and limited information on the status of the resource prospect. Hence, new information would be necessary to influence the current trend. Through this thesis, we attempted to fill this gap by conducting the first magnetotelluric study on Svalbard.

Magnetotellurics is a geophysical method that uses natural source electromagnetic signals to probe the earth from shallow tens of meters to hundreds of kilometres below the surface, given measurements of the electric and magnetic field components in the appropriate period range are taken at the surface. Besides its popularity in crustal to astenospheric depth study [Jones, 1999, Korja, 2007, Meqbel et al., 2014], magnetotellurics has a broad application in geothermal and other resource explorations [Spichak and Manzella, 2009, Streich et al., 2010, Muñoz, 2014, Samrock et al., 2015].

The MT acquisition system has low environmental impact. Therefore, the method is well suited for deployment on places such as Svalbard, comprising tundra and a fragile environment. Among other advantages of MT, one can mention the large penetration depth, the simplicity and lower cost of deployment relative to other comparable geophysical techniques. From MT data valuable information can be obtained to complement seismic and extend often depth limited shallow geophysical and borehole data sets. In this respect, the new MT data would be significant to reveal the crustal scale geological framework in the region, which

mainly inferred from seismic and gravity studies in the past [Haremo et al., 1990, Eiken, 1994, Bergh et al., 1997, Harland, 1997, Bergh and Grogan, 2003].

Magnetotellurics is considered suitable for geothermal mapping due to the relation between subsurface conductivity and geothermal attributes, such as fluid content, porosity and temperature. Although not sufficient to make a conclusion, a potential geothermal reservoir often coincides with a low resistivity zone that MT has a high sensitivity for [Spichak and Manzella, 2009]. In the case of Svalbard, it is in general the proximity of the archipelago to the mid-Atlantic spreading ridge, the presence of uplifted and fractured structures, shallow basin fills, thick sedimentary covers, major deeply-seated fault zones and extensive horst-graben (basin) systems are among the features assumed to provide the region with characteristics favouring technologically accessible geothermal resources.

Interpretation of MT data involves solving the inverse problem and searching for a certain resistivity model of the earth fitting reasonably the observed data at the surface. However, the nature of the MT inverse problems is usually ill-posed. Therefore, often supported by a priori information, a careful and systematic investigation of the candidate models is necessary to obtain a stable and a geologically meaningful resistivity model.

1.2   List of contributions

   I Beka, Thomas I; Smirnov, Maxim; Bergh, Steffen G; Birkelund, Yngve. The First Magnetotelluric Image of the Lithospheric Scale Geological Architecture in Central Svalbard, Arctic Norway. Polar Research 2015, 34, 26766

  II Beka, Thomas I; Smirnov, Maxim; Birkelund, Yngve ; Senger, Kim; Bergh, Steffen G. 3-D Magnetotelluric imaging of Central Svalbard, Norway. (in review with Tectonophysics).

 III Beka, Thomas I; Bergh, Steffen G.; Maxim; Birkelund, Yngve. Magnetotelluric signatures of the complex Tertiary fold-thrust belt and extensional fault architecture beneath the Brøgger peninsula, Svalbard. (in review with Polar Reserarch)

 IV Beka, Thomas I; Senger, Kim; Autio, Uula; Smirnov, Maxim; Birkelund, Yngve. Integrated electromagnetic data investigation of a Mesozoic CO2 storage target reservoir-cap rock succession, Svalbard (manuscript).

Other works carried out in the course of the PhD study but not included in the dissertation for evaluation:

- Beka, Thomas I; Smirnov, Maxim; Birkelund, Yngve. Reconnaissance Geothermal Resource Assessment Using Magnetotelluric Imaging on Svalbard, Norway. Proceedings of World Geothermal Congress 2015, Melbourne, Australia.

- Beka, Thomas I; Birkelund, Yngve; Smirnov, Maxim. Correlating magnetotelluric sounding with borehole data for geothermal parameter characterization in Sulitjelma area, Norway. Proceedings of the European Geothermal Congress 2013, Pisa, Italy.

- Beka, Thomas I; Birkelund, Yngve. Rapid well log data lithology discrimination by means of informed clustering. (manuscript to be reviewed and resubmitted).

1.3   Organization of the thesis

Magnetotellurics is a wide topic involving various fields, a very basic theory and assumptions behind the method are discussed in Chapter 2. In chapter 3, we present the geology of Svalbard focusing on the studied areas in central and northwest Spitsbergen, also by indicating the relevant thermal aspects that make probing the area with MT data appropriate. In chapter 4, we describe in brief the techniques applied during the MT field data acquisition and processing. We conclude the chapter by discussing our fieldwork strategy and experience. As the parameter of interest is not readily available from measured data, thus inversion is necessary, which we briefly over-viewed in Chapter 5. Chapter 6 starts by giving a short overview of the four papers and roles of the authors involved. The remaining part of the chapter is dedicated to the original manuscripts. A concluding remark linking the main accomplishments of the thesis is given in Chapter 7, where we also commented on future outlook. Finally, it should be noted that some minor edition is made to this printed version of the manuscript after the dissertation was approved by the evaluation committee.

Chapter 2

The basics of magnetotellurics

The magnetotelluric method is a geophysical exploration technique governed by the principles of electromagnetic induction [Tikhonov, 1950, Cagniard, 1953]. Using MT, one can probe subsurface resistivity from a few tens of meters to several hundred kilometres, on the basis measured time varying natural source electric and magnetic fields at the surface. The variational fields employed as signal sources have meteorological and geomagnetic origins, and prevail typically in the period range between 10^{-3} - 10^5 s [Vozoff, 1991]. The short period signal below 1 s comes from worldwide lightning discharges, whereas the lower frequency signal $<$1 Hz (i.e. longer period signal) has its origin in the complex interaction of the solar wind with the earth's magnetic field.

The penetration depth for MT investigation is controlled by the employed sounding period and the underlying subsurface resistivity condition. This relation is embodied in the skin depth formulation, which describes the distance over which the amplitude of a propagating electromagnetic (EM) field attenuates from its surface value by $1/e$ ($\approx$37%) as it diffuses downward within the conductive earth:

$$\delta = 503\sqrt{\rho T}, \qquad (2.1)$$

where δ is the skin depth in meter, ρ describing the underlying average resistivity in Ωm and T denoting the period in seconds. Based on the recorded period bandwidth, a survey can be classified as a broadband magnetotelluric (BMT) for 0.001 - 1000 s or if the data is recorded between 1 - 10000 s as a long-period magnetotelluric (LMT) data study [Chave and Jones, 2012]. In this thesis, studying the BMT data range would be sufficient, as the main interest is exploring the hidden geothermal potential in the crust.

MT is proposed independently by Tikhonov [Tikhonov, 1950] and Cagniard [Cagniard, 1953]. The method assumes that the source field is a plane wave, generated far away in ionosphere so that it can be considered as uniform when incident at the surface [Vozoff, 1972]. A fraction of the incident wave penetrates into the earth vertically in z direction, by inducing electrical currents called telluric, which in turn produce secondary magnetic fields. The second assumption of MT states that no EM field is generated in the earth, i.e. the source is only of external origin. This means differing secondary fields are induced only as a result of contrast in the underlying subsurface structure. Thus by studying the relation between simultaneously measured electric and magnetic fields, one can derive the resistivity structure of the subsurface at a given frequency. The third assumption states the role of the displacement current neglected ($\omega\epsilon \ll \sigma$) for the period range operable by magnetotellurics, the so called quasi-static approximation. With this assumption the propagation of EM waves into the earth is treated as a diffusive process. The basic theory of the technique is discussed briefly in the following sections.

2.1 Propagation of electromagnetic wave in the earth

The underlying physics necessary to formulate magnetotellurics is found in the Maxwell's equations, which serve to describe the induction and propagation of electromagnetic waves in a magnetisable and polariseable medium without its own electric or magnetic source:

$$\nabla \cdot \overrightarrow{D} = \varrho, \tag{2.2}$$

$$\nabla \cdot \overrightarrow{B} = 0, \tag{2.3}$$

$$\nabla \times \overrightarrow{E} = -\frac{\partial \overrightarrow{B}}{\partial t}, \tag{2.4}$$

$$\nabla \times \overrightarrow{H} = \overrightarrow{j} + \frac{\partial \overrightarrow{D}}{\partial t}. \tag{2.5}$$

Where $\overrightarrow{D}$ (C/m²) denotes the electric displacement, ϱ (C/m³) the electric charge density, $\overrightarrow{B}$ (T) the magnetic induction, $\overrightarrow{E}$ (v/m) the electric field, $\overrightarrow{H}$ (A/m) the magnetic field intensity, and $\overrightarrow{j}$ (A/m³) represents the electric current density. Following the interpretation in Chave and Jones [2012], Coulomb's law in Equation 2.2 describes the divergence of electric fields from a electric charges, Gauss's law in Equation 2.3 states the absence of magnetic monopoles, Faraday's law in Equation 2.4 tells about the induction of closed loop time-varying magnetic fields along the path of an electric field, and Ampere's law in Equation 2.5 says that

the vector sum of electric currents ($\overrightarrow{j}$) and time-varying electric fields generate a circulating magnetic field. The EM fields satisfying Equation 2.2 - 2.5 are quasi-static, meaning their spatial distribution does not change much, acting statically despite their time-dependency.

Moreover, in a linear and isotropic medium the scalar material properties of dielectric permittivity $\epsilon = \epsilon_0 \epsilon_r$ in (As/Vm), magnetic permeability $\mu = \mu_0 \mu_r$ in (Vs/Am), and electrical conductivity σ (S/m) can be employed to relate the vectorial quantities of Equations 2.2 - 2.5:

$$\overrightarrow{D} = \epsilon \overrightarrow{E}, \tag{2.6}$$

$$\overrightarrow{B} = \mu \overrightarrow{H}, \tag{2.7}$$

$$\overrightarrow{j} = \sigma \overrightarrow{E}, \tag{2.8}$$

Equation 2.8 describes Ohm's law, which states that a material must have non-zero conductivity to allow electric fields to pass through it. The relative-permittivity denoted by ϵ_r and permeability by μ_r are important respectively if the material under study is an ore body and if the displacement current is considered, which both can be overlooked in MT case. Thus we can simply approximate $\epsilon \approx \epsilon_0 = 8.85.10^{-12}$ As/Vm and $\mu \approx \mu_0 = 4\pi 10^{-7}$ Vs/Am.

To derive the diffusive nature of the magnetotellurics governing equations, we start first by rewriting Ampere's law using the constitutive relations of Equation 2.6 - 2.8:

$$\nabla \times \overrightarrow{B} = \mu\sigma\overrightarrow{E} + \mu\epsilon\frac{\partial \overrightarrow{E}}{\partial t}. \tag{2.9}$$

Applying the curl operator allows to obtain the differential equation of the quasi-static field satisfying Equation 2.4, ultimately aiming at expressing the equation in terms of only the electric field,

$$\nabla \times \nabla \times \overrightarrow{E} = -\frac{\partial}{\partial t}(\nabla \times \overrightarrow{B}), \tag{2.10}$$

The vector relation $\nabla(\nabla \cdot \overrightarrow{E}) - \nabla^2 \overrightarrow{E}$ can be used in place of the curl curl operation of Equation 2.10. There is no charge accumulation ($\varrho = 0$) in a homogeneous conductive medium, which leads to $\nabla \cdot \overrightarrow{E} = 0$ when Equation 2.2 is written using the constitutive relation of Equation 2.6. We reformulate Equation 2.10 by

substituting Equation 2.9 and considering time independent material properties (μ, ϵ & σ):

$$\nabla(\nabla \cdot \overrightarrow{E}) - \nabla^2 \overrightarrow{E} = \nabla^2 \overrightarrow{E} = \mu\sigma\frac{\partial \overrightarrow{E}}{\partial t} + \mu\epsilon\frac{\partial \overrightarrow{E}^2}{\partial^2 t}. \tag{2.11}$$

Similarly, if we follow the above steps to find the curl of Equation 2.9 (Ampere's law), we would get the following:

$$\nabla^2 \overrightarrow{B} = -(\mu\sigma + \mu\epsilon\frac{\partial}{\partial t})(\nabla \times \overrightarrow{E}) = \mu\sigma\frac{\partial \overrightarrow{B}}{\partial t} + \mu\epsilon\frac{\partial \overrightarrow{B}^2}{\partial^2 t}, \tag{2.12}$$

as $\nabla \cdot \overrightarrow{B}$ is zero by Equation 2.3. Equation 2.11 & 2.12 have the form of a telegrapher's equation with a diffusive (conduction current) and a wave (displacement current) terms, sufficient to describe electromagnetic field propagation in a homogeneous medium, such as in the earth [Zhdanov and Keller, 1994]. Assuming harmonic time dependence ($e^{-i\omega t}$) electric and magnetic fields with the angular frequency $\omega = 2\pi f$, we express Equation 2.11 & 2.12 in frequency domain:

$$\nabla^2 \overrightarrow{E} = -i\omega\mu\sigma\overrightarrow{E} + \omega^2\mu\epsilon\overrightarrow{E}, \tag{2.13}$$

$$\nabla^2 \overrightarrow{B} = -i\omega\mu\sigma\overrightarrow{B} + \omega^2\mu\epsilon\overrightarrow{B}. \tag{2.14}$$

Since $\omega\epsilon << \sigma$ even when the maximum frequency (10^4 Hz) for magnetotellurics operation is accounted for, we ignore the displacement current (wave) terms from Equations 2.13 & 2.14. This is the quasi-static assumption of magnetotellurics that is crucial to describe the diffusive nature the EM propagation in the earth:

$$\nabla^2 \overrightarrow{E} = \kappa^2 \overrightarrow{E}, \tag{2.15}$$

$$\nabla^2 \overrightarrow{B} = \kappa^2 \overrightarrow{B}. \tag{2.16}$$

Here $\kappa = \sqrt{-i\omega\mu\sigma}$ represents the complex wave number, using Euler's form we can expand $\sqrt{-i} = (e^{-i\frac{\pi}{4}})^{\frac{1}{2}} = \pm(1-i)\frac{1}{\sqrt{2}}$, then we have

$$\kappa = \pm(1-i)\sqrt{\frac{\omega\mu\sigma}{2}}. \tag{2.17}$$

Considering depth (z) dependence as EM fields propagate vertically in the earth through diffusion, we can write the following solutions to Equations 2.15 & 2.16:

$$\vec{E} = \vec{E}_1 \, e^{(-1+i)\sqrt{\frac{\omega\mu\sigma}{2}}z} + \vec{E}_2 \, e^{(1-i)\sqrt{\frac{\omega\mu\sigma}{2}}z}. \tag{2.18}$$

$$\vec{B} = \vec{B}_1 \, e^{(-1+i)\sqrt{\frac{\omega\mu\sigma}{2}}z} + \vec{B}_2 \, e^{(1-i)\sqrt{\frac{\omega\mu\sigma}{2}}z}. \tag{2.19}$$

As a boundary condition we expect the field to vanish as $z \longrightarrow \infty$, which can be fulfilled if $\vec{E}_2$ and $\vec{B}_2$ are zero, meaning that the second terms disappear from the solutions. The second boundary condition, i.e, $z = 0$, yields the surface values of the fields, i.e. $\vec{E}_1$ and $\vec{B}_1$. The proposed solutions with out the second term have an imaginary component describing an oscillatory propagation and a real term describing a depth dependent exponential dissipation of the EM field flowing in the earth [Weaver, 1994]. The real part of the solution serves to derive the skin depth (ϱ) we presented in Equation 2.1. This can be done by considering the ratio of the real part $\vec{E}_1(z = \varrho)/\vec{E}_1(z = 0)$ to find the distance the field uses to attenuate with $1/e$. If we solve the ratio for ϱ, we obtain $\sqrt{2/\omega\mu\sigma}$, which is the same as Equation 2.1 given that $\mu \approx \mu_0 = 4\pi 10^{-7}$, $\rho = 1/\sigma$ and $T = 1/f$.

2.2 Transfer functions of magnetotelluric response

Components of sounded EM fields at a given frequency can be linearly related to one another through the magnetotelluric transfer function, also called impedance tensor [Berdichevsky, 1960] and a geomagnetic transfer function (tipper) [Vozoff, 1972]. Due to the assumption of a homogeneous plane wave source, the transfer functions are considered independent of source morphology. Thus they describe only contrasts of the underlying resistivity condition.

The 2×2 impedance tensor, $\boldsymbol{Z}$, relates the horizontal electric and magnetic fields,

$$\begin{bmatrix} E_x(\omega) \\ E_y(\omega) \end{bmatrix} = \begin{bmatrix} Z_{xx} & Z_{xy} \\ Z_{yx} & Z_{yy} \end{bmatrix} \begin{bmatrix} B_x(\omega) \\ B_y(\omega) \end{bmatrix}. \tag{2.20}$$

The complex impedance tensor (with real and imaginary parts) can be interpreted through its magnitude (apparent resistivity) and phase parameters component wise ($ij = xx, xy, yx, yy$):

$$\rho_a^{ij}(\omega) = \frac{\mu}{\omega} \mid Z_{ij}(\omega) \mid^2, \tag{2.21}$$

$$\phi_{ij}(\omega) = \arctan \frac{Im Z_i j(\omega)}{Re Z_i j(\omega)}. \tag{2.22}$$

The apparent resistivity denoted by ρ_a (Ωm) represents the average resistivity in a volume of subsurface at a particular frequency, and the impedance phase ϕ in degree describes the phase difference between the electric and magnetic field giving additional information on the resistivity structure [Simpson and Bahr, 2005].

At a particular frequency, an anomalous induced vertical magnetic field component is linearly related with horizontal inducing magnetic fields through the complex tipper vector, $\boldsymbol{T}(\omega)$:

$$B_z(\omega) = \begin{bmatrix} T_x(\omega) & T_y(\omega) \end{bmatrix} \begin{bmatrix} B_x(\omega) \\ B_y(\omega) \end{bmatrix}. \tag{2.23}$$

Tippers appear due to the presence of H_z in a multidimensional earth or at boundary of ocean and land. The property of tipper is often graphically illustrated with induction vectors, serving to characterize the directions of a lateral conductive anomaly, and define the direction of the geoelectric strike in 2D earth. The induction vectors can be expressed either in Wiese convention [Wiese, 1965] with arrows pointing away from a lateral conductivity increase or in Parkinson convention [Parkinson, 1962] with arrows pointing towards the conductivity increase. The magnitude ($|Re(T)|$) and angle ($Re(T)_\theta$) of the induction vector's real parts are defied as follows:

$$|Re(T)| = \sqrt{Re(T_x)^2 + Re(T_y)^2} \tag{2.24}$$

$$Re(T)_\theta = arctan\frac{Re(T_{zy})}{Re(T_{zx})}. \tag{2.25}$$

2.3 Magnetotelluric models of earth induction

Depending on the underlying spatial resistivity distribution, earth's geomagnetic induction is described by a one-, two- or three-dimensional (1D, 2D or 3D) form of the impedance tensor [Vozoff, 1972].

In 1D earth, resistivity varies only vertically in z direction with depth. In this case, the impedance tensor ($\boldsymbol{Z}$) shown in Equation 2.20 has zero diagonal entries ($Z_{xx} = Z_{yy} = 0$), whereas the off-diagonal entries coupling the orthogonal electric and magnetic fields have equal magnitude with a sign change ($Z_{xy} = -Z_{yx}$), meaning a phase lag of 180 degrees between the xy and yx components.

$$\phi_{yx}(\omega) = \phi_{xy}(\omega) - \pi. \tag{2.26}$$
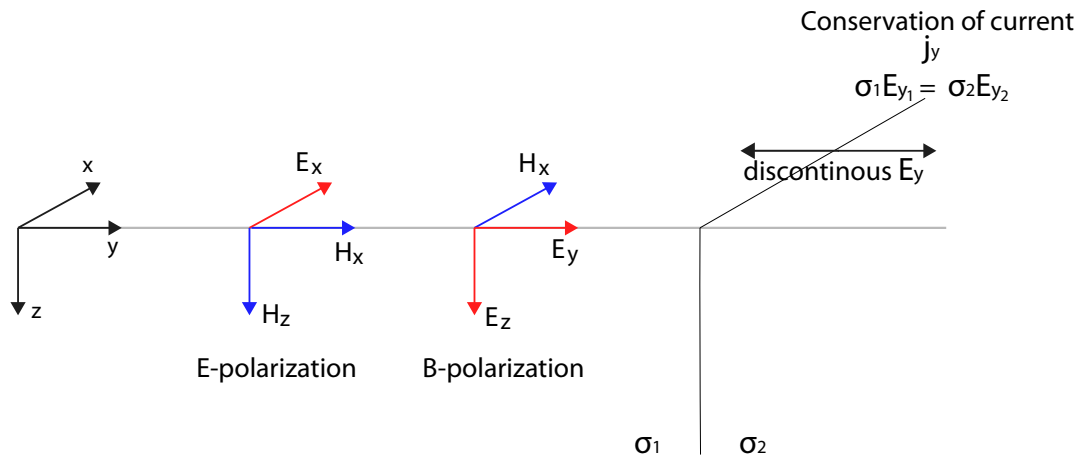
FIGURE 2.1: 2D resistivity model with two sections of unequal conductivity to illustrate the concept of E- and B-polarizations. The lateral contact strikes along the x-direction, with minor modification from Simpson and Bahr [2005].

In 1D case, there is no induced magnetic field in z-direction, thus the tipper vector in Equation 2.23 doesn't exist.

In a 2D earth, resistivity is constant in one horizontal direction known as the geo-electric strike, aligned parallel to the x-axis. Resistivity varies in the other horizontal direction (y) and vertically along z. At a vertical interface between two zones of differing resistivity, electric fields (E_y) become discontinuous to guarantee conservation of current across the boundary (Equation 2.8), while the other EM field components remain continuous.

Following the description in Simpson and Bahr [2005], for an infinity long body (larger than skin depth) along the strike direction, no variations along x ($\frac{\partial}{\partial x} = 0$) are expected. In a perfectly 2D condition the electric and magnetic fields are mutually orthogonal and can be decoupled into electric field parallel to strike (E-polarization) and magnetic field parallel to strike (B-polarization). The electric field parallel to strike (E_x) induces only magnetic fields B_y (perpendicular to strike) and B_z in the vertical plane, whereas magnetic field parallel to strike (B_x) induces only perpendicular electric fields (E_y) and E_z (see Fig. 2.1). The E-polarization (Transverse electric (TE) mode) describing current flow parallel to strike and the B-polarization (transverse magnetic (TM) mode) describing current flow perpendicular to strike have the following sets of relations derived from the Maxwell's equations (2.5 & 2.4):

$$\frac{\partial B_z}{\partial y} - \frac{\partial B_y}{\partial z} = \mu\sigma E_x,$$

$$\frac{\partial E_x}{\partial z} = -i\omega B_y, \tag{2.27}$$

$$\frac{\partial E_x}{\partial y} = i\omega B_z.$$

$$\frac{\partial E_z}{\partial y} - \frac{\partial E_y}{\partial z} = -i\omega B_x,$$

$$\frac{\partial B_x}{\partial z} = \mu\sigma E_y, \tag{2.28}$$

$$-\frac{\partial B_x}{\partial y} = \mu\sigma E_z.$$

The B-polarization tends to resolve lateral resistivity contrasts sharper but act less effective resolving along strike variations. The impedance tensor of a 2D earth in strike coordinate (x aligned with strike) has zero off-diagonal entries:

$$\boldsymbol{Z}_{2D} = \begin{bmatrix} 0 & Z_{xy} \\ Z_{yx} & 0 \end{bmatrix}. \tag{2.29}$$

The Z_{xy} uses sets of fields (E_x,B_y) associated with TE-mode and Z_{yx} employs E_y,B_x from the TM-mode. Induction vectors are available only for TE mode, as there is no a vertical magnetic component for the TM-mode.

For 3D earth, the impedance tensor has full entries that are independent of one another ($Z_{xx} \neq$ -Z_{yy}, $Z_{xy} \neq Z_{yx}$), and resistivity can vary along the x, y and z directions.

2.4   Data dimensionality and distortion

Often MT field data are not recorded in the strike coordinate frame and their off diagonal entries are non-zero. To recover the 2D impedance tensor in Equation 2.29 the impedance tensor $\boldsymbol{Z}$ is rotated by a strike angle θ to the strike coordinate frame using a rotation matrix $\boldsymbol{R}$:

$$\boldsymbol{Z} = \boldsymbol{R}(\theta)\boldsymbol{Z}_{2D}\boldsymbol{R}^{\intercal}(\theta), \tag{2.30}$$

where T denotes matrix transpose and the matrix $\boldsymbol{R}$ is given by

$$\boldsymbol{R} = \begin{bmatrix} \cos\theta & \sin\theta \\ -\sin\theta & \cos\theta \end{bmatrix}. \tag{2.31}$$

There are several techniques to check the dimensionality weather data can be described with a 2D model and to determine an appropriate strike [e.g. Swift, 1967, Zhang et al., 1987, Bahr, 1988, Caldwell et al., 2004]. However, it should be noted that there is a 90 degrees ambiguity on the actual strike direction when the strike is determined via impedance tensor rotation, as rotating the tensor with 90 degrees leads to swapping the off-diagonal elements [Simpson and Bahr, 2005]. The ambiguity can be resolved using tipper vectors, which in 2D case are oriented perpendicular to the strike direction, collectively.

The rotationally invariant misfit, Swift skew (κ) [Swift, 1967], provides a parameter describing the extent to which the underlying structure can be considered as 2D

$$\kappa = \frac{|\ Z_{xx} + Z_{yy}\ |}{|\ Z_{xy} - Z_{yx}\ |}. \tag{2.32}$$

If κ is larger than 0.2 it indicates a departure from a 2D condition. When the Swift skew is small, it is suggested that strike can be derived as the angle (θ) minimizing the sum of the diagonal $\boldsymbol{Z}$ entries. However, the Swift skew is sensitive to galvanic effect [Bahr, 1991], which may lead to erroneous strike estimation.

A galvanic effect is a non-inductive distortion occurring due to presence of shallow and small scale anomalies compared to the skin depth of the smallest period measured [Berdichevsky and Dmitriev, 1976, Jiracek, 1990, Wannamaker et al., 1984]. The phenomena arise due to a non-time dependent charge accumulation at interfaces of local bodies with contrasting conductivity while current attempts to keep continuous flow across the discontinuity, eventually creating a secondary electric field superimposed distorting the primary field either by enhancing or diminishing it. Magnetic fields are less affected by galvanic distortion [Jiracek, 1990, Agarwal and Weaver, 2000]. In a 1D situation, galvanic distortion is recognized as a frequency-independent off-set (static shift) on the apparent resistivity, and which leave the phase parameters non-affected [Chave and Jones, 2012]. However, although a parallel shift between the xy and yx polarizations of the apparent resistivity indicates static shift, the converse may not be necessarily true.

A model to compute a phase-sensitive strike is proposed by Bahr [1988]. The method claims that in a regional strike coordinate system the phase of elements in a column of the impedance tensor is the same ($\mathrm{Re}Z_{xx}/\mathrm{Im}Z_{xx} = \mathrm{Re}Z_{yx}/\mathrm{Im}Z_{yx}$), and

a strike can be derived by rotating the tensor to satisfy the condition in one of the impedance columns [Simpson and Bahr, 2005]. Together with the phase-sensitive strike, Bahr [1988] introduced a phase-sensitive skew parameter (η, 3D/2D skew), to evaluate the extent to which the impedance tensor can be described through decomposition into a local 3D heterogeneities (a galvanic non-inductive response) and a regional 2D structure [Simpson and Bahr, 2005],

$$\eta = \frac{\sqrt{|[D_1, S_2] - [S_1, D_2]|}}{|D_2|} \tag{2.33}$$

where $S_1 = Z_{xx} + Z_{yy}$, $D_1 = Z_{xx} - Z_{yy}$, $S_2 = Z_{xy} + Z_{yx}$, $D_2 = Z_{xy} - Z_{yx}$ and the notation [a,b]=Re(a)Im(b)-Re(b)Im(a). The modified impedances S_1, S_2, D_1 and D_2 [Vozoff, 1991, Simpson and Bahr, 2005] are derived through expanding the right side of Equation 2.30. The 3D/2D skew provides a necessary but not a sufficient condition to regard an underlying structure as 2D if the parameter is smaller than 0.3 [Bahr, 1991, Ledo et al., 2002]. The 2D/3D skew is insensitive to galvanic distortion, however, it overlooks variation of strike with period and from site to site [Smirnov and Pedersen, 2009]. When η is larger than 0.3, it may indicate a prevailing 3D effect [Bahr, 1991, Ledo et al., 2002].

The Q-function analysis [Zhang et al., 1987, Smirnov and Pedersen, 2009, Cherevatova et al., 2015] assumes that it would be possible to find a dominant strike direction consistent at period ranges along a profile, if the data have a 2D structure. The strike is estimated through minimizing an objective function (Q) comprising column-wise square normalized misfit between $\boldsymbol{Z}$'s diagonal and off-diagonal elements [Smirnov and Pedersen, 2009]. Furthermore, the square root of Q_{ij} enables to test whether the strike assumption is acceptable for a local site (i) at a given period (j)

$$Q_{ij} = \frac{1}{4\sigma^2_{xy_{ij}}} |Z_{xx_{ij}} - \zeta_i Z_{yx_{ij}}|^2 + \frac{1}{4\sigma^2_{yx_{ij}}} |Z_{yy_{ij}} - \gamma_i Z_{xy_{ij}}|^2 . \tag{2.34}$$

The parameters ζ and γ represent galvanic distortions and have a physical meaning if a regional strike is present. 5% error floor is assigned to Z_{xy} and Z_{yx}, since their error estimates are often small [Zhang et al., 1987, Smirnov and Pedersen, 2009]. The weighing factor in each column (σ_{xy} or σ_{yx}) is drawn from the variance of the corresponding off-diagonal element. Under the assumption that the column-wise $\boldsymbol{Z}$ misfit is normally distributed with zero mean and its corresponding variance, Q_{ij} would follow a χ^2 distribution and $Q^{1/2}$ would have one as its expected value [Smirnov and Pedersen, 2009]. If the proposed strike is not suitable for $\boldsymbol{Z}_{ij}$, the situation would be indicated by large $Q^{1/2}$ (see Paper II for examples).
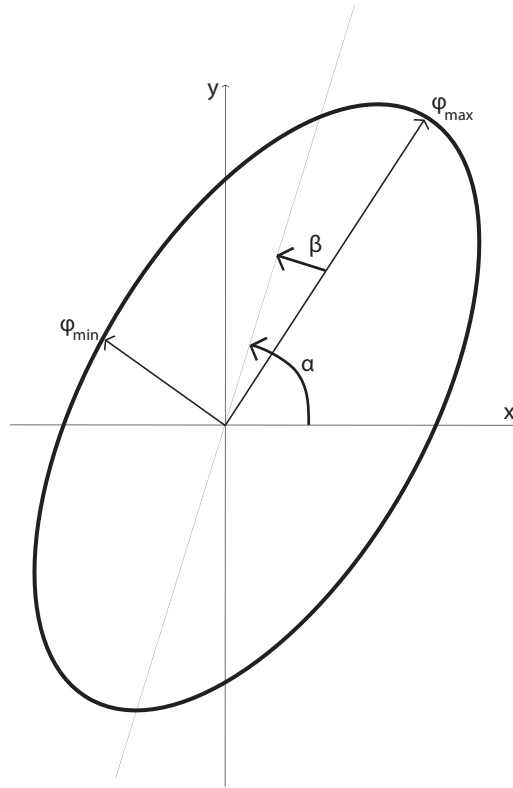
FIGURE 2.2: Graphical representation of the MT phase tensor, redrawn from Caldwell et al. [2004]. α defines the tensor's dependence on the coordinate system, the skew angle β measures the tensor asymmetry and $\alpha - \beta$ defines the direction of the ellipse's major axis.

The MT phase tensor is immune to distortion [Caldwell et al., 2004]. It ($\boldsymbol{\Phi} = \boldsymbol{X}^{-1}\boldsymbol{Y}$) is derived from the impedance tensor's real ($\boldsymbol{X}$) and imaginary ($\boldsymbol{Y}$) parts. $\boldsymbol{\Phi}$ can be expressed in a decomposed form in terms of three coordinate invariants (i.e. the tensor's maximum ϕ_{max}, minimum ϕ_{min} & the skew angle β) together with an auxiliary angle α defining the tensor's dependence on the coordinate frame:

$$\boldsymbol{\Phi} = \begin{bmatrix} \phi_{11} & \phi_{12} \\ \phi_{21} & \phi_{22} \end{bmatrix} = \boldsymbol{R}^{\mathsf{T}}(\alpha - \beta) \begin{bmatrix} \phi_{max} & 0 \\ 0 & \phi_{min} \end{bmatrix} \boldsymbol{R}(\alpha + \beta). \qquad (2.35)$$

$\boldsymbol{R}(\alpha + \beta)$ is a rotation matrix and T denotes its transpose. α and β are defined by:

$$\begin{aligned} \alpha &= \frac{1}{2} arctan(\frac{\phi_{12} + \phi_{21}}{\phi_{11} - \phi_{22}}) \\ \beta &= \frac{1}{2} arctan(\frac{\phi_{12} - \phi_{21}}{\phi_{11} + \phi_{22}}). \end{aligned} \qquad (2.36)$$

The skew angle β measures the tensor's asymmetry. In the case of a 2-D earth,

β less than three degrees could be used as a subjective criterion [Booker, 2014]. Graphical illustration of the tensor can be made with an ellipse (see Figure 2.2). Where the ellipse's major and minor axes depict the tensors principal axes and orientation of the major axis is specified by $\alpha - \beta$, which also gives an estimate of the geo-electric strike [Caldwell et al., 2004, Booker, 2014].

2.5   Electrical conductivity in geological materials

The role of MT is mapping subsurface electrical conductivity, a property defining materials ability to carry current. Earth materials have resistivity values that span over several orders of magnitude(see Figure 2.3), and they may behave as: *i*) a conductor (10^{-8}- $10^{-}5$ Ωm), *ii*) a semiconductor (10^{-5}-10^7 Ωm) or *iii*) an insulator ($>10^7$ Ωm). However, the conduction structure can be influenced or controlled by factors like temperature, presence of volumetrically minor but electrically highly conductive minerals (e.g. ore mineral & graphite) and the tectonic situation. Current flows through a medium due to charge carriers mobility under an applied electric field. Depending on the type of the involved charge carrier and its mobility, the mechanism of the conduction can be subdivided as an electronic or electrolytic type. In metallic conductors such as graphite, current is transported by free electrons, and the conductivity decreases with increasing temperature. Most rocks such as sulfides and ignous types can be considered as semiconductors, having a temperature dependent conductivity that can be modelled by the Arrhenius equation:

$$\sigma = \sum_{i=1}^{N} \sigma_i \mathrm{e}^{-\frac{-E_i}{kT}}, \tag{2.37}$$

where the summation is made over conduction related to impurity, intrinsic and ionic processes, each dominating when the temperature is $<$600 °C, 600 - 1100 °C and $>$1200 °C, respectively [Stegena, 1976]. E_i is the activation energy corresponding to the underlying conduction mechanism, k is the Boltzmann's constant and T is the absolute temperature. The effect of temperature on conductivity particularly predominates at large depth, where the temperature is high enough to influence the mobility and energy state of charged particles. Based on laboratory data, there is a consensus on the role of temperature to enhance conductivity at lithospheric depth, however the matter is unsettled for astenospheric depth [Chave and Jones, 2012] due to the double role of dissolved hydrogen in olivine to enhance conductivity [Karato, 1990, Yoshino et al., 2006, 2008].

Graphite is an efficient electronic conductor and its films are often raised as a reason for high bulk conductivity in lower crust and lithospheric mantle, particularly
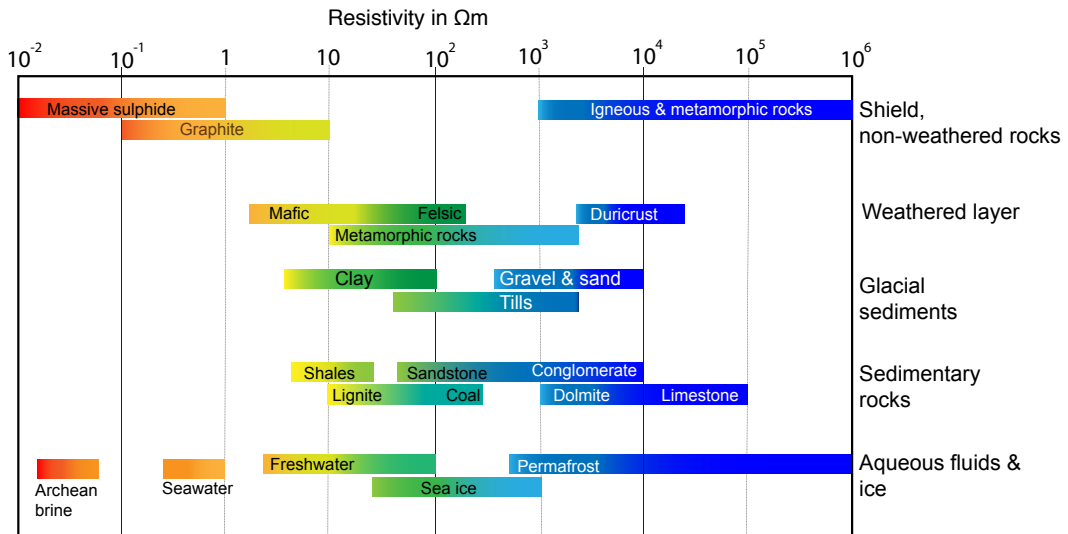
FIGURE 2.3: Typical electrical resistivity ranges for earth materials and ac-
queous, from Palacky [1987] with minor modification.

in sheared zones. However, to maintain increased bulk resistivity at a regional
level, large scale interconnections of graphite films would be necessary, and there
is a limited evidence whether this is possible to preserve over geological time scales
[Wannamaker, 2000]. On the other hand, in highly deformed crustal shear zones,
increased pressure and carbon are mentioned aiding to connect graphite networks,
with a direction of conduction aligned to the shearing direction [Shankland et al.,
1997, Chave and Jones, 2012].

A small amount of fluid (aqueous or molten material) in cracks within the crust can
largely increase the bulk conductivity due to electrolytic conduction as current is
carried by ions. The relation between pore fluid and bulk conductivity is described
by Archie's law [Archie, 1942], which can be written in a simplified form as [Chave
and Jones, 2012]:

$$\rho_m = A\rho_f \varphi^{-m}, \tag{2.38}$$

where ρ_m is the bulk resistivity, ρ_f is the resistivity of the pore fluid, φ is the
porosity, m is a cementation exponent that controls the bulk conductivity and
describes the degree of interconnection of the pore fluid, and A is an empirically
fitting factor to describe the degree of saturation. When clay mineral is present,
it can enhance bulk conductivity due to electrical double layer at the interface
of the clay mineral and water, serving as additional pathway for current flow
[Waxman et al., 1968]. For instance, sandstones and shales act as less resistive
than dolmite and limestones due to higher clay content and porosity. Moreover, the

bulk conductivity will increase with salinity of the pour fluid, as this brings more ions to carry current. On the other hand, resistivity may rise due to compaction, and reduction of porosity.

The conductivity of a partially melting mantle material is estimated to lie between 1 - 10 S/m, and the value can be affected by temperature, pressure, water content, melt fraction, interconnection geometry, and composition of the material. Partial melt is considered prevalent in asthenosphere; however, there are also evidences for its presence in volcanic areas, geothermal zones, and in tectonically active crust [Li et al., 2003, Didana et al., 2014].

To conclude, the tectonic history of a survey area needs to be taken into consideration when interpreting crustal conductors [Duba et al., 1994], as the resistivity can be affected by tectonics related factors such as up-welling partial melt, content of aqueous fluid, metallic, carbon or sulphide minerals [Chave and Jones, 2012].

Chapter 3

Geological setting

3.1 Tectonic history and regional structure

Svalbard is located in the northwestern corner of the Eurasian plate, separated from Greenland by the North Atlantic mid-ocean ridge and a major transform plate boundary known as the Hornsund-De Geer Fault Zone [Faleide et al., 2008]. From the Devonian trough the Cretaceous periods, Svalbard was part of the Old Red continent that consisted of Greenland, Eurasia and North America [Elvevold et al., 2007]. Some 65 million years ago, at the transition from the Cretaceous to the Tertiary period, the Eurasian and North American plates started drifting away from each other. As part of the rifting, the Greenland continental plate pressed on Svalbard at an angle, while Svalbard was sliding past the northern part of Greenland along a transform plate boundary fault with dextral offset of the mid-Atlantic ridge. This caused intense transpressional uplift, folding and thrusting along the western section of Spitsbergen. This belt of contractional deformation is named as the Tertiary fold- and-thrust belt (see Paper III), and it is characterized by sharp and jagged mountain peaks along the coast. At the same time in central Spitsbergen west of the Tertiary belt, the crust subsided forming a large N-S trending bay, Forland basin, with thick sedimentary strata of sandstones, mudstones and coal deposits. The majority of the coal deposit and the mining activity (settlements) are found in this section of Spitsbergen, known as the Central Tertiary Basin (CTB). Besides the younger uplifted mountain ranges formed during the Tertiary period, there are also remains from the older Precambrian (> 540 Ma) and Caledonian (500-400 Ma) mountain ranges on Svalbard.

The regional structure of Svalbard is characterized by segmented blocks and basins bounded by major fault systems, such as the Cenozoic Hornsund-De Geer fault

zone, the Billefjorden fault zone (BFZ) and the Lomfjorden fault zone (LFZ) [Harland, 1997, Dallmann, 1999, Bælum and Braathen, 2012]. Most of the present day major fault systems were formed in the Caledonian through Paleozoic era but were later reactivated as compressional faults in the Paleocene-Eocene period [Bergh et al., 1997, Harland, 1997], causing extensive uplift and exhumation in certain domains. The closeness to the mid-Atlantic spreading ridge and presence of widespread fault systems, it is not uncommon to register notable seismic incidents on the Svalbard region [Mitchell et al., 1990, Pirli et al., 2010].

3.2   Bed rock and lithostratigraphy

The geology of Svalbard displays diverse and well exposed segments that can be traced back to different stages of earth's history [Harland, 1997, Elvevold et al., 2007, Worsley, 2008]. In general, the stratigraphy of Svalbard is that of a crystalline and metamorphic basement of Precambrian and Caledonian rocks overlain by a thick composite sedimentary sequence starting with Devonian and Carboniferous basin fills, and up to 3.5 km thick successive Permian through Eocene platform deposits [Harland, 1997, Dallmann et al., 2002]. Notable thickness variations exist in the west-central and eastern parts of Svalbard for the Devonian basin deposits, but also for Carboniferous strata adjacent to reactivated block-boundary faults such as the BFZ, the LFZ [Harland, 1997], faults adjacent to the St. Jonsfjorden Trough in northwestern Spitsbergen [Steel and Worsley, 1984] as well as the Inner Hornsund Trough in southern part of Spitsbergen. Notably also in the central parts of Spitsbergen, there are thick uniform and widespread sequences of Permian carbonates, limestones, dolomites and evaporite [Worsley, 2008]. In the Cretaceous, weak crustal extension led to the intrusion of a major dolerite dyke-sill swarm along fractures and bedding surfaces, and the volcanic activity associated caused high heat flow in the archipelago.

3.3   The thermal aspect of the geology

In geological terms a geothermal reservoir can be thought of as a section of the upper crust, which is hotter than its surrounding [Stegena, 1976]. Svalbard has properties that can be considered indicative of technologically exploitable thermal potentials due to its proximity to the mid-oceanic ridge, adjacent transform plate boundary as well as its numerous deeply-seated fault zones. The heat flow rate in the region is considerably larger than what is commonly found in Northern Europe [Khutorskoi et al., 2009, Slagstad et al., 2009]. For instance, 130 mW/m^2 is

recorded in an area believed to be affected by a late Cenozoic crustal uplift [Vågnes and Amundsen, 1993], and more recently 80 mW/m^2 is reported as a steady borehole heat flow rate in Sysselmannbreen area of central Spitsbergen [Pascal et al., 2011]. Borehole studies have also indicated thermal gradients exceeding 40°C/km beneath the permafrost in northeastern flank of the CTB, where CO_2 geological storage is planned [Elvebakk, 2010]. Adjacent to a Quaternary age volcanic system on Spitsbergen one can find the northern most documented thermal springs in the world, the Trollkildene and Jotunkildene, lying along the north-south (N-S) trending Breibogen fault [Banks et al., 1998, Treiman, 2012]. Other discovered thermal fields are linked to a network of major N-S trending fault zones that are parallel to the Cenozoic Hornsund-De Geer fault zone (HFZ) transform plate boundary [Faleide et al., 2008, Dallmann, 1999]. These thermal springs seen at various locations of northwestern and southern Spitsbergen indicate a continuously high geothermal gradients along the uplifted Tertiary fold-and-thrust belt [Dallmann, 2007].

Chapter 4

Magnetotelluric field data

The magnetotelluric method requires simultaneous measurements of the time varying natural source EM field components of the $H_x(t), H_y(t), E_x(t), E_y(t)$ and $H_z(t)$ at the surface. As a standard practice, the vertical electric field (E_z) signal is not measured, as air is a perfect insulator and E_z can be very weak. The H_z component is required for tipper estimation (Equation 2.23), thus it may not be necessary to measure it at every site. In the following paragraphs we discuss briefly our acquisition, data processing and fieldwork strategies.

4.1   Data acquisition and processing

The data presented in this thesis are measured in the broadband range covering the period range 0.001 - 1000 s. For the acquisition we employed the MTU2000 system, developed at Uppsala university (Sweeden) and later assembled at Oulu University (Finland) [Smirnov et al., 2008].

In this acquisition system, magnetic field components are measured with broadband induction coils magnetometers LEMI-120 that are produced in Ukraine. An example of an installed H_z component is shown in Figure 4.1a. Electric fields are determined from measured potential difference ($\Delta V/d = E$) using two orthogonal dipoles typically having ca. 100 m long wire and a non-polarisable Pb-PbCl$_2$ electrode at each end. The dipoles are aligned with magnetic north-south and east-west directions, and are buried in the ground to reduce temperature variation, ensure wet environment and low contact resistance. Pb-PbCl$_2$ are in general considered stable and diurnal temperature variations were minimal in the studied locations. However, getting a reasonable contact resistance in the range of few tens of kΩ was challenging during our winter measurements, where the ground

FIGURE 4.1: Induction coil magnetometer and electrode installations. (a) A coil installed to measure the H_z component. (b) Due to frozen surface and permafrost, often challenging to get a good contact to the ground. (c) An electrode being buried in an ice pool filled with a salty solution.

was sealed by snow, frozen ice and permafrost sequentially. A high contact resistance can lead to attenuated high frequency (shorter period) electric signals, as the recording system may act as a resistor-capacitor low-pass filter due to coupling between the high contact resistance and the distributed capacitance of the dipole wires [Chave and Jones, 2012]. This may reduce the amplitude of apparent resistivity at short periods and may distort the phase response [Evans et al., 2005]. As a rule of thumb to reduce the effect of high contact resistance, it is recommended that LfR_c is kept below two, where in this case L is the dipole wire length in km, f frequency in kHz, and the contact resistance (R_c) is given kΩ [Zonge and Hughes, 1985, Chave and Jones, 2012]. Planting the electrodes in a ground ice pools filled with a water solution of 15% or more salt helped to achieve a stable contact resistance in the range of 5 - 40 kΩ (see the picture in Figure 4.1c). Nevertheless, still 20 - 40 kΩ may reduce the recorded signal by 1 - 2 percent, due to capacitance effect, which depends on the cable and the set-up used. Our set-up estimates that capacitance is very low that it does not affect, while voltage divider of the input amplifier resistance and contact resistance matter. The system has a 2 MΩ input, which means at 20 kΩ input resistance, one percent of the signal will be lost.

At each station, data were recorded for a period of about 24 hours to be able to average over multiple cycles (20 or more) in order to achieve accurate estimate of a signal at a given frequency. 20 Hz sampling was made continuously through out the entire duration of the acquisition, and in parallel 1000 Hz sampling (AMT recordings) was carried out for 2 hours starting at midnight anticipating low industrial noise in this time interval, although this may not fully represent the situation on Svalbard where the industrial noise is in at the general minimum.

Data are digitized and stored using a recorder from Earth Data Limited., which is capable of operating for long term and has the capacity to handle high sampling rates reaching 3000 Hz as well as dual burst mode recordings. As a stable power source a standard 12 V car battery was used. The data logger is connected to a GPS receiver for precise determination of a station location and to make accurate time synchronization between stations that are operating simultaneously. After configuring the recorder, a field laptop is employed to monitor the data quality and check the status of the equipment operation in situ.

During data acquisition, we installed two to three instruments at a time at different locations and recorded data simultaneously. The purpose is to use the sites later during data processing as mutual remote references, assuming that a separation distance in the ranging of hundred meters to few kilometres would be sufficient to be out of a noise range that can be generated through wind and ground motion,

while measuring essentially the same signal. DC electric trains are not present in the studied region. On the other hand, despite source field treat when measurement is deployed in auroral zone, we have not experienced irregular behaviour in the data that we can relate to electro-jet activity.

In general, the target of MT data processing is reducing the measured raw time-series electric and magnetic field vectors to reliable transfer functions, which are frequency domain spectral ratios between the field components [Chave and Jones, 2012]. However, estimation of the transfer functions such as the impedance and tipper is often hampered by the noise involved and data outliers. Thus several statistical processing techniques such as the least-square and the robust processing methods are commonly used to remove noise from MT data [Egbert and Booker, 1986, Chave et al., 1987]. Moreover, remote referencing is employed to eliminate bias arising due to a local and uncorrelated noise at one station using a signal (usually magnetic) from another site (the so called remote site) using techniques of spectral analyses [Gamble et al., 1979].

For the material presented in this thesis, the practical processing of the measured time-series electric and magnetic signals is performed using the Robust Remote Reference Algorithm of Smirnov [2003], where final results were derived through averaging multiple remote reference estimates in the robust statistical manner [Smirnov and Pedersen, 2009]. The code is developed to provide optimal protection against the effect of outliers and large errors.

4.2 Fieldwork

As part of this thesis we acquired MT data at different parts of Svalbard through three field expeditions carried out between the year 2013 and 2015. The location of the measured sites is indicated on Figure 4.2 and further detail on each of the expeditions is given in the following paragraphs:

i) FW-I represents 24 MT sites measured east of Longyearbyen in Adventdalen during the summer of 2013. These MT data were the first ever collected on Svalbard and the sites were distributed along a profile having 500 m as an average site to site separation. The main constraint of this campaign was mobility. The road crossing the measured valley is quite limited (ca. 10 km) and driving all-terrain vehicles on the tundra is prohibited, other than snowmobiles when the surface is covered by snow. This constraint ultimately lead to scheduling the upcoming field campaigns to winter, as there is no better road facility other than the above mentioned on in the region. For winter measurement, the month of
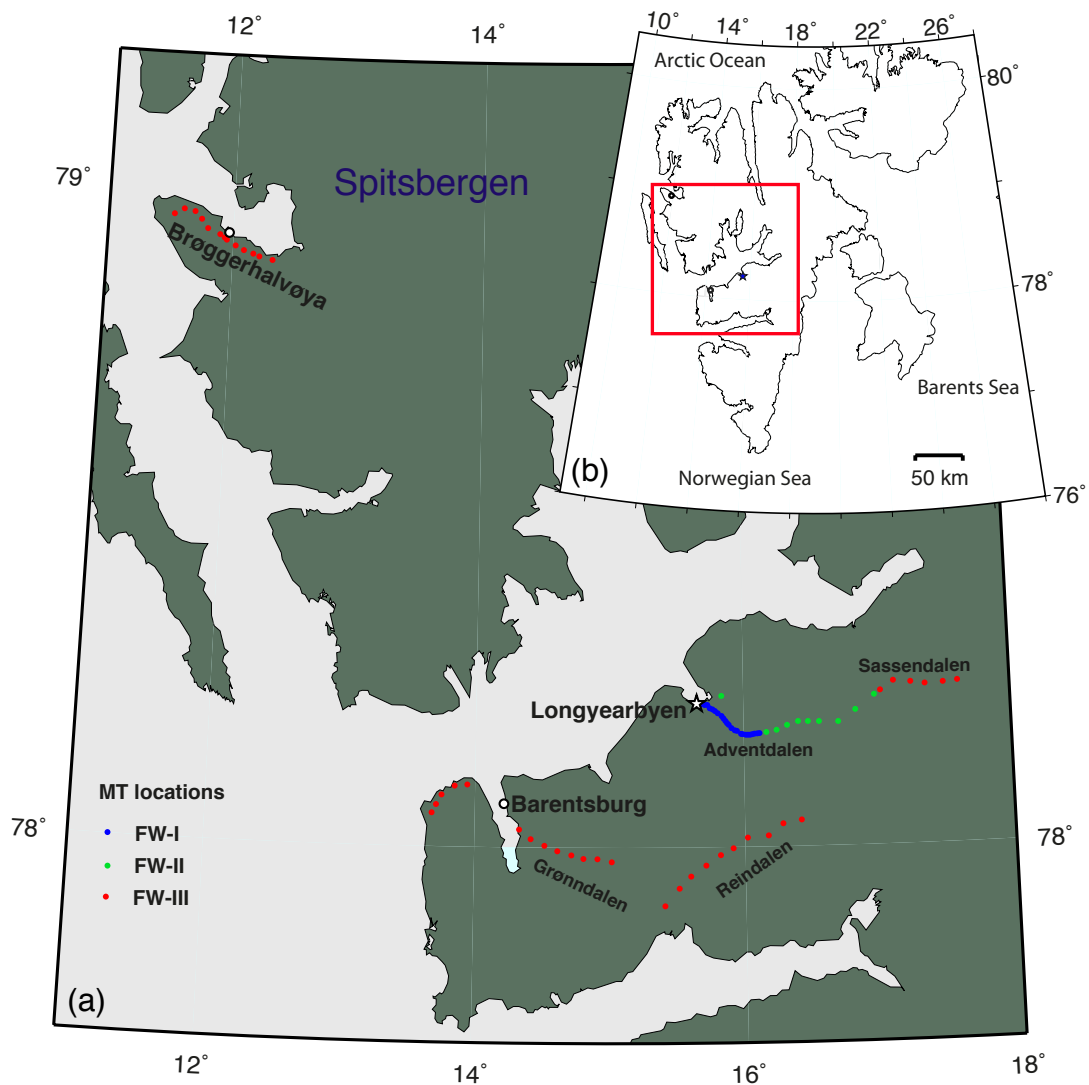
FIGURE 4.2: Survey locations. (a) The location of the 78 MT sites measured on Spitsbergen. The first fieldwork (FW-I) was deployed in August 2013, FW-II in May 2014 and FW-III was carried out in May 2015. (b) The Svalbard archeplago, with the MT studied section framed in red.

May was found to be a suitable candidate, since there would often be some snow cover while at the same time moderate temperature can be achieved for proper instrument functioning.

ii) FW-II represents a profile measured between lower Adventdalen and western Sassendalen in May 2014 using snowmobiles to access the sites. With a crew of two, we measured a total of eleven stations separated on average by 2 km from each other. During this expedition, we also measured the vertical magnetic field at seven of these stations. The main challenges of the winter campaign was deep

snow at some locations which prohibited access to ground to bury electrodes, or when ground was found obtaining a moderate contact resistance was challenging due to ice and permafrost.

iii) FW-III was the largest field campaign we carried out, with three to four crew members at a time, between April and May 2015. We collected data from 42 sites (including the tipper at several stations) by making profiles in Sassendalen, Reindalen, Grønndalen, across Isfjord-radio and on the Brøgger peninsula. In addition, about 16 time-domain electromagnetic (TEM) sites were measured in Adventdalen. The TEM data are included in Paper IV.

During the planning process, we also considered vicinity to inhabited areas since the main motivation of the study is geothermal potentials. In this respect, we also attempted to focus on areas with some geological manifestations favouring a geothermal anomaly, such as faults, anomalous heat flow, graben features and so on. Besides, we made careful evaluation of the logistics before making a decision on a survey location, particularly since batteries serving as power sources needed to be regularly recharged and changed due to the cold condition. Lastly, we also tried not to deploy measurement along shore lines when possible to avoid potential coastal effect.

Chapter 5

Overview of the data inversion

In most geophysical studies, the data that are observed (measured) are not the actual desired parameters, and finding the parameter of interest involves solving forward and inverse problems. Often the forward computations are performed as part of the inversion procedure. In the case of magnetotellurics, the parameter of interest is subsurface resistivity, whereas the measured parameters are EM fields at the surface that are converted through data processing into transfer functions, relating the field components. Forward modelling via Maxwell's equations enables to predict responses at the surface that would be possible to observe from an assumed earth resistivity model at a given frequency and location. The converse is the inverse problem, which provides a method to infer a subsurface model from the actually observed data at the surface.

If we denote the observed data with a column vector of N elements $\boldsymbol{d} = [d_1, d_2 ... d_N]^\mathsf{T}$ having the corresponding uncertainties of $\boldsymbol{e} = [e_1, e_2 ... e_N]^\mathsf{T}$, and assuming that the earth model can be discretised as the parameter vector $\boldsymbol{m} = [m_1, m_2 ... m_M]^\mathsf{T}$; the inverse problem can be stated as

$$\boldsymbol{d} = \boldsymbol{F}(\boldsymbol{m}) + \boldsymbol{e}. \tag{5.1}$$

Where $\boldsymbol{F}$ is a forward operator projecting elements from the $M \times M$ model space $\mathcal{M}$ to the $N \times N$ data space $\mathcal{D}$, and can be expanded in the form of $\boldsymbol{F}(\boldsymbol{m}) = [F_1(\boldsymbol{m}), F_2(\boldsymbol{m}) ... F_N(\boldsymbol{m})]^\mathsf{T}$. The aim with solving the inverse problem is finding a model whose forward responses best fit (reproduce) the observed data within corresponding error, through minimizing a function that measures the discrepancy between the observed and predicted data. Using a least square formulation the data misfit $\boldsymbol{d} - \boldsymbol{F}(\boldsymbol{m})$ can be expressed as a weighted L_2-norm of residuals assuming that they obey Gaussian statistics [Menke, 1989]:

$$\psi(\boldsymbol{m}) = \lVert \boldsymbol{W}\boldsymbol{d} - \boldsymbol{W}\boldsymbol{F}(\boldsymbol{m}) \rVert^2 = [\boldsymbol{d} - \boldsymbol{F}(\boldsymbol{m})]^\intercal \boldsymbol{W}[\boldsymbol{d} - \boldsymbol{F}(\boldsymbol{m})], \qquad (5.2)$$

where $\boldsymbol{W}$ is a positive definite diagonal weighting matrix of size $N \times N$, and it can be eliminated from the definition of $\psi(\boldsymbol{m})$ through rescaling of the data and the forward mapping [Egbert and Kelbert, 2012]. Equation 5.2 is a least-square objective function of a linearised inverse problem [Menke, 1989], which can be minimized by taking its derivative with respect to m_j and setting the result to zero. However, the MT forward operator $\boldsymbol{F}$ is non-linear due to the nature of the product relation between conductivity and the EM fields in the Maxwells' equations (Equations 2.13 & 2.14) defining it, i.e., $F[a\boldsymbol{m_1} + b\boldsymbol{m_2}] = aF(\boldsymbol{m_1}) + bF(\boldsymbol{m_2})$ can not be satisfied for arbitrary real numbers a & b [Chave and Jones, 2012]. $\boldsymbol{F}$ can be linearised through Taylor expansion about some trial model $\boldsymbol{m}_k$, and approximation ($\overline{\boldsymbol{F}}$) is made using the first two terms:

$$\overline{\boldsymbol{F}}(\boldsymbol{m}) = \boldsymbol{F}(\boldsymbol{m}_k) + \frac{\partial \boldsymbol{F}(\boldsymbol{m}_k)}{\partial \boldsymbol{m}_k}(\boldsymbol{m} - \boldsymbol{m}_k) = \boldsymbol{F}(\boldsymbol{m}_k) + \boldsymbol{J}\delta\boldsymbol{m}. \qquad (5.3)$$

In Equation 5.3, $\delta\boldsymbol{m} = \boldsymbol{m} - \boldsymbol{m}_k$ are small perturbations in the model. $\boldsymbol{J}$ is the Jacobian or the sensitivity matrix of $N \times M$ partial derivatives $\partial F_i(\boldsymbol{m})/\partial m_j$, where $i = 1, 2...N$ & $j = 1, 2...M$. The Jacobian describes the sensitivity of the predicted data due to the small perturbation in the model.

Using the linearised form of $\boldsymbol{F}$ (Equation 5.3) and minimizing Equation 5.2 yields the following solution [e.g. Menke, 1989, Chave and Jones, 2012, Meqbel, 2009]:

$$\delta\boldsymbol{m} = (\boldsymbol{J}^\intercal \boldsymbol{J})^{-1}\boldsymbol{J}^\intercal \boldsymbol{r}, \qquad (5.4)$$

where $\boldsymbol{r} = (\boldsymbol{d} - \boldsymbol{F}(\boldsymbol{m}_k))$. Equation 5.4 is the Gauss-Newton solution of the unconstrained least square problem. Since it is obtained using the Taylor approximated $\boldsymbol{F}$ (Equation 5.3), the solution can be optimized through iterative techniques. However, in most MT data inversion schemes, the number of model parameters is often much larger than the size of data parameters ($N \ll M$), thus the solution in Equation 5.4 can not be determined uniquely. Setting a constraint on the objective function is used as a strategy to tackle the ill-posedness to seek a regularized and stable solution [Tikonov and Arsenin, 1977]:

$$\Psi(\boldsymbol{m}) = \psi(\boldsymbol{m}) + \lambda\Omega(\boldsymbol{m}), \qquad (5.5)$$

where $\Omega(\boldsymbol{m})$ is a stabilizing functional serving to penalize unwanted property of $\boldsymbol{m}$ [Chave and Jones, 2012], and λ is a trade-off (regularizing) parameter. A small λ puts more weight on fitting the data, whereas a large λ emphasises on

model smoothness before the data misfit. Thus an optimal λ should be chosen to maintain adequate data fit without compromising for model roughness. Moreover, the regularized objective function can be expresses as:

$$\Psi(\boldsymbol{m}) = [\boldsymbol{d} - \boldsymbol{F}(\boldsymbol{m})]^{\mathsf{T}} \boldsymbol{C}_d^{-1} [\boldsymbol{d} - \boldsymbol{F}(\boldsymbol{m})] + \lambda [\boldsymbol{m} - \boldsymbol{m}_0]^{\mathsf{T}} \boldsymbol{C}_m^{-1} [\boldsymbol{m} - \boldsymbol{m}_0], \qquad (5.6)$$

where the weight matrix in Equation 5.2 is represented by $\boldsymbol{C}_d^{-1}$, which is the inverse data covariance having the data errors $(e_1^{-1}, e_2^{-1} ... e_N^{-1})$ along its diagonal entries, to account for contributions by individual errors to the total prediction error. $\boldsymbol{m}_0$ is a prior (first guess) model parameter, and $\boldsymbol{C}_m^{-1}$ is the inverse model covariance matrix helping to define the expected magnitude and smoothness of model variations relative to $\boldsymbol{m}_0$ [Siripunvaraporn and Egbert, 2000, Kelbert et al., 2014].

5.1   Occam approach for a linearized problem

Minimizing the regularized objective function $\Psi(\boldsymbol{m})$ in the vicinity of $\boldsymbol{m}_k$ due to small perturbations $\Delta \boldsymbol{m} = \boldsymbol{m}_{k+1} - \boldsymbol{m}_k$ provide $M \times M$ system of normal equations:

$$(\boldsymbol{J}^{\mathsf{T}} \boldsymbol{C}_d^{-1} \boldsymbol{J} + \lambda \boldsymbol{C}_m^{-1}) \Delta \boldsymbol{m} = \boldsymbol{J}^{\mathsf{T}} \boldsymbol{C}_d^{-1} (\boldsymbol{d} - \boldsymbol{F}(\boldsymbol{m}_k)) - \lambda \boldsymbol{C}_m^{-1} (\boldsymbol{m}_k - \boldsymbol{m}_0). \qquad (5.7)$$

Equation 5.7 can be solved for $\Delta \boldsymbol{m}$ as a trial solution for the damped least square problem [Egbert and Kelbert, 2012], which can be improved iteratively. For magnetotellurics data several techniques are used to solve the Equation 5.7, which allow repeating the process with different λ to minimize the data misfit until a desired stationary level is achieved.

In the Occam approach [Constable et al., 1987], an iterative sequence of approximate solutions for Equation 5.7 is expressed through:

$$\boldsymbol{m}_{k+1}(\lambda) = \boldsymbol{m}_k + \Delta \boldsymbol{m} = (\boldsymbol{J}^{\mathsf{T}} \boldsymbol{C}_d^{-1} \boldsymbol{J} + \lambda \boldsymbol{C}_m^{-1})^{-1} \boldsymbol{J}^{\mathsf{T}} \boldsymbol{C}_d^{-1} \tilde{\boldsymbol{d}}_k + \boldsymbol{m}_0 \qquad (5.8)$$

where $\tilde{\boldsymbol{d}}_k = \boldsymbol{d} - \boldsymbol{F}(\boldsymbol{m}_k) + \boldsymbol{J}(\boldsymbol{m}_k - \boldsymbol{m}_0)$. The Occam procedure involves a two step process: bringing the misfit down to a desired level, and while keeping the misfit at the desired level achieving a small model norm through varying λ [Parker, 1994]. In the process, the trade-off parameter is employed in each iteration both as a step length control and a smoothing parameter. In practice, Equation 5.8 is solved for a series of trial λ values and the obtained prediction error from each is evaluated through solving the forward problem. Finally, the model with the minimum misfit

is preserved and passed to the next iteration [e.g. Siripunvaraporn and Egbert, 2000].

5.2 Data space scheme

The Occam procedure can also be implemented using a data space scheme, by transforming the inverse problem solution method from the model space to the data space [Siripunvaraporn and Egbert, 2000, Siripunvaraporn et al., 2005]:

$$\boldsymbol{m}_{k+1} - \boldsymbol{m}_0 = \boldsymbol{C}_m \boldsymbol{J}^\mathsf{T} \boldsymbol{\beta}_{k+1} \tag{5.9}$$

where

$$\boldsymbol{\beta}_{k+1} = (\boldsymbol{J} \boldsymbol{C}_m \boldsymbol{J}^\mathsf{T} + \lambda \boldsymbol{C}_d)^{-1} \tilde{\boldsymbol{d}}_k. \tag{5.10}$$

In Equation 5.10, $\boldsymbol{J} \boldsymbol{C}_m \boldsymbol{J}^\mathsf{T}$ is the data space cross product matrix, having the size of $N \times N$. With this, the dimension of the system of equations to solve is reduced compared to the practice in the standard model space Occam procedure (Equation 5.8), where $M \times M$ model space cross product matrix ($\boldsymbol{J}^\mathsf{T} \boldsymbol{C}_d^{-1} \boldsymbol{J}$) is employed. Thus the inverse problem is focused on searching for N unknown $\boldsymbol{\beta}_{k+1}$ expansion coefficients of the basis function $\boldsymbol{C}_m \boldsymbol{J}^\mathsf{T}$ in Equation 5.9. Notice also that $\boldsymbol{C}_m$ is used in data space approach not its inverse as in the model space case. This provides a possibility to include prior information such as bathymetry that should be fixed in model [Siripunvaraporn and Egbert, 2000]. Rebocc (reduced basis Occam) is a variant of the data space Occam approach [Siripunvaraporn and Egbert, 2000], allowing to speed up the inversion and reduce memory requirement. In this approach, it is assumed that a satisfactory approximation to the solution can be achieved from a subset of the data space, considering redundant basis functions as the MT data is expected to be smooth and redundant.

5.3 Inversion of the non-linearized problem

A solution for the regularized objective function (Equation 5.7) can be searched directly using the nonlinear conjugate gradient (NLCG) approach [Newman and Alumbaugh, 2000, Rodi and Mackie, 2001], through evaluating the gradient with respect to model parameters, $\partial \Psi(\boldsymbol{m})/\partial \boldsymbol{m}$. By this, NLCG avoids the need for repeated linearised inversions [Chave and Jones, 2012]. For the NLCG method the explicit use of the Jacobian matrices is unnecessary [Avdeev, 2005]. The memory and computational advantages associated with not operating with J makes the NLCG a good option for solving 3D problems often involving a large number

of model parameters [Meqbel, 2009]. However, practical computation should be carried out in a parallelized system or CPU clusters [Avdeev, 2005]. Moreover, NLCG requires more steps to achieve convergence compared to the Gauss-Newton approaches [Avdeev, 2005, Meqbel, 2009].

Chapter 6

Papers

6.1   Overview of the papers and roles

Paper I.   The first magnetotelluric image of the lithospheric-scale geological architecture in central Svalbard, Arctic Norway.

The focus of this paper is 2D modelling of the MT data we collected during FW-I and partly during FW-II. In the paper, the implication of the result on the lithospheric scale geology is discussed.

My contribution to this paper starts from planning the surveys, and carried out the data collection and processing together with Dr. Maxim Smirnov, and finally analysed and model the data. I wrote the first draft of the manuscript, which the co-authors/supervisors greatly helped to improve.

Paper II.   3-D Magnetotelluric Imaging of Central Svalbard, Arctic Norway.

In paper I adequate attention was not given to the 3D behaviour of the data that we discussed in the paper. Thus by including additional sites and tipper from FW-II, we modelled the data in 3D. After providing a detailed discussion on the data analyses, we used this paper to suggest and test out various inversion strategies and parameter combinations using the parallel version of the ModEM code, to help improve the output that can be achieved from MT field data. We also used the paper to discuss how we adopted a detailed bathymetry of the region into our 3D model grid.

My contribution to this paper is designing the inversion strategies and implementing them on a parallel computing facility, and writing the first draft of the

manuscript. The co-authors contributed by providing several feedbacks on the manuscript and by helping with interpretations.

Paper III. Magnetotelluric signatures of the complex Tertiary fold-thrust belt and extensional fault architecture beneath the Brøgger peninsula, Svalbard.

In this paper we presented new MT data from Brøgger peninsula, on which Ny-Ålesund is located. After modelling the data in 2D and in 3D following the strategies discussed in Paper-II, we discussed the architecture of the crustal geology by making comparison between the MT result and previous geological studies. In this case the MT data served to reaffirm previous assertions made on the Tertiary deformed bed rock strata in the area. Moreover, the MT models provided a fresh view on the deeper structural architecture of the geology along a WNW-ESE transect.

My contribution to Paper III is planning the survey, taking part in the data collection and processing with Dr. Maxim Smirnov, analysing and modelling the data, and writing most of the first draft of the manuscript. The geological interpretations are written in collaboration with Prof. Steffen Bergh. Finally, Dr. Maxim Smirnov and Dr. Yngve Birkelund helped to improve the manuscript by providing several comments.

Paper IV. Integrated electromagnetic data investigation of a Mesozoic CO2 storage target reservoir-cap rock succession, Svalbard.

The purpose of this manuscript is to combine part of the MT data from FW-I in audio period range with the newly collected TEM data during FW-III. The result of the combined data is presented in the context of the targeted CO_2 geological storage reservoir in Adventdalen. We also used this paper to integrate the EM results with existing seismic and borehole data, and performed synthetic test on assumed geological scenarios of the reservoir structure.

This manuscript is more of a collaborative work between Uula Autio, Dr. Senger and myself. The TEM data were collected by Autio and myself during FW-III. Autio processed, 1D modelled and prepared the TEM data for joint inversion with audio range MT data. We implemented inversions on the combined data, and I interpreted the data and wrote most of the manuscript. Dr. Kim Senger contributed by describing the geology and the CO2 storage project. He also suggested the geological scenarios to test with synthetic inversion, which I implemented and experimented with. The remaining co-authors contributed by providing feedbacks. Finally, Dr. Maxim Smirnov has contributed by sharing scripts we used during data analyses and processing while working towards the above four Papers.

Chapter 7

Conclusions

The main accomplishment of this thesis is its successful application of the magnetotelluric method on the remote but geologically important Svalbard, where previous knowledge of the geology depended mainly on surficial, seismic and gravity studies. In this respect, the thesis contributes considerably with new electromagnetic data and helps to reveal the framework of the crustal scale geology in the region.

7.1   Main contributions

1. *Inputs in terms of characterizing the geology:*

• From the new MT data we derived crustal scale 2D and 3D resistivity models, that helped to constrain better the surficial bedrock and the crustal scale geological architecture of the studied areas on Svalbard. The stratigraphic framework derived from the MT models is discussed in more detail in Paper I, II and III.

The final models of the data 2D determinant and 3D inversions resolved mostly comparable resistivity structures and geometries. However, for the data acquired in Adventdalen and Sassendalen (Paper II), a more complex near surface (<1.5 km) resistivity structure resolved by 3D inversion suggesting a higher frequency of fractures, localized faults and thick intrusive dyke swarms in the sub-horizontal and less deformed Mesozoic platform cover deposits. This result is in good agreement with previous geological data and models of the area. The MT data from the Brøgger peninsula northwest Spitsbergen, on the other hand, indicated a more deformed subsurface architecture. This is well justifiable if the location of the area within the Tertiary fold- and thrust belt as well as the impact of the later Tertiary

oblique-normal faulting are considered. The MT data in this section imaged an interplay between repeated basement-involved fold-thrust belt and successive steeply dipping oblique-normal fault structures, for instance the Scheteligfjellet fault. In this respect, the MT enabled to unravel the deeper and complex architecture of the fold-thrust belt along a WNW-ESE profile.

2. *On data analysis, modelling and 3D inversion strategy:*

• We applied 3D inversion on a crooked profile and suggested various inversion strategies to improve the output from such a limited data set. This theme is addressed in Paper II.

2D models could not explain the MT data adequately, therefore, we employed the determinant data for 2D inversion as a solution. In Paper II, we emphasised on the reason why 3D inversion of the crooked profile is necessary to justify the 2D results. For this we dedicated the first part of Paper II to in-depth data analyses. Also in Paper II, we experimented with various inversion strategies using a high performance computing facility. In the process, we devised an interface to extract bathymetric information from a recently compiled Arctic sea depth chart [Jakobsson et al., 2012] in a manner compatible to 3D MT model grids. Our results from testing different inversion settings indicated the cruciality of appropriately choosing and tuning together the starting model, the data error floor and the model regularization in order to achieve optimum benefit from MT field data. Through 3D inversion, we also enabled to fit impedance components that were out of quadrant and obtained an overall satisfactory data fits. In Paper III, we exploited the 3D inversion strategies that we proposed and tested in Paper II.

3. *On inference of lithosphere thickness:*

• Following a one dimensional approach, we derived a regional level resistivity stratigraphy through averaging the final 2D model. From the result we estimated a thinned lithosphere thickness in the range between ca. 55 - 100 km.

The estimated thickness is found to be one possible explanation for the elevated surface heat flow (ca. 60 - 90 mW/m^2) registered in the region. The estimate also indicated coincidence with calculated depths of the thermal lithosphere heat-base boundaries for a partially melting mantle (see Paper I) under the assumption that a thermally defined lithosphere base follows a 1300 °C isoline.

4. *On CO$_2$ reservoir characterization and permafrost:*

• By combining EM sounding data (AMT and TEM) with seismic and geotechnical information, we demonstrated the advantage of employing an integrated

approach when characterizing a CO_2 geological storage reservoir. This is a theme of Paper IV.

Through jointly inverting part of the MT data in audio period range (0.003 - 1 s) together with TEM measurements (0.01 - 10 ms), we presented a 2D resistivity model displaying a laterally constrained and a highly conductive anomaly at ca. 400 - 500 m depth. At the same depth scale a parallel seismic section indicated a concealment and core samples suggested a highly fractured decollement zone. The inversion of the combined data also estimated permafrost that extended down to ca. 200 m below the surface. However, synthetic model tests suggested that this may have been exaggerated by tens of meters, due to a screening effect resulting from the presence of a thin conductive layer in the near surface (ca. 10 - 25 m). A similar characteristic of the near surface is also mentioned in Paper I, where the permafrost was overshadowed in some sections beneath the fluvial plain of Adventdalen, presumably due to presence of large amounts of conductive wet oceanic sediments and clay. Furthermore, in Paper IV presents several synthetic model examples to investigate the expected geological scenarios of the CO_2 reservoir structure, where we also illustrated the diffusive nature of a propagating EM field, the permafrost thickness and the challenge to image thin layers at increasing depth especially when they have high resistivity.

5. *On geothermal resource prospect:*

• The MT study has enabled to suggest two prospect sites in a reconnaissance sense that potentially may hold accessible geothermal heat in Paper I - III. These locations are situated in the vicinity of the settled areas in Ny-Ålesund and Longyearbyen. Thus investigating the sites more closely and developing the resources may lead to socio-economic and environmental benefits in future.

On the Brøgger peninsula, aquifers are imaged at ca. 2 - 6 km below the surface within upraised horsts of the pre-Devonian basement, mainly in the vicinity of the sub-vertical Scheteligfjellet fault. In the same area, there are also evidences for a lateral and sub-vertical cap-rock sealing surrounding the aquifer systems. Thus this area seems to be the most appropriate among the studied sections in the northwest for further investigation of exploitable geothermal heat.

For the profile adjacent to Longyearbyen, a Devonian basin fill is imaged as a conductive upper crustal anomaly. These conductive sections are laterally and vertically bounded by resistive rocks, creating conducive environment for deep geothermal heat storage. This is an encouraging scenario for a low-enthalpy geothermal development. Moreover, the prospect site has proximity to a targeted subsurface for CO_2 geological storage. Hence, following a concerted approach in the studies of the geothermal and CO_2 reservoirs can be advantageous; since better a mobility

can be achieved using a less viscose supercritical CO_2 ($ScCO_2$) as a working fluid than through water in a tight geothermal reservoir.

7.2   Future work and recommendations

The next step in the development of the current work is linking different profiles from central Spitsbergen and preparing a 3D model. We believe the result from that will bring a more consolidated regional 3D image of the central Spitsbergen.

On the other hand, there are several issues we did not have the capacity to adequately address during the course of this thesis, and which could be an extension of the current work. Although we did not find evidence for irregular and unusual behaviour in our data set that we can relate to the source field, the potential threat is there. Presumably the source effect can be more prominent in long period MT data, and a proper attention needs to be given to this topic in future.

When it comes to data acquisition, Svalbard is suitable in winter times especially for installing magnetic sensors and the vertical coil due to abundant snow and little wind, see Figure 4.1. However, the situation is the opposite when it comes to electrodes due to high contact resistance, potentially everywhere. In this respect, we have had a great success to bring down the contact resistance by burring electrodes in an ice pool containing a highly saturated salty solution. In this respect experimenting with electrodes that can easily adopt to the frozen condition would be a great contribution to facilitate future MT studies on permafrost and icy ground elsewhere.

The result of our study encourages application of more electromagnetic techniques (passive and active) to further investigate the suggested geothermal locations as well as the CO_2 geological storage sites. Particularly shallow EM methods should be tested on Svalbard, as the level of industrial noise contaminating high frequency signal is quite minimal.

There are several sites of geological interest on Svalbard that are not well constrained at deeper level, which MT could offer assistance to investigate. Nevertheless, careful evaluation of the logistics and the topography should be given consideration when planning future MT study on Svalbard, since more than 50% of the archipelago is still under glaciers. In addition, accessing a reliable station for recharging power sources or just a laptop can be challenging especially in the remote sections during winter, as batteries discharge quicker. Finally, magnetotellurics is not still a well established methodology in Norway, and we hope our accomplishment will motivate others to consider the method.

Bibliography

Agarwal, A., Weaver, J., 2000. Magnetic distortion of the magnetotelluric tensor: a numerical study. Earth, planets and space 52, 347–353.

Archie, G.E., 1942. The electrical resistivity log as an aid in determining some reservoir characteristics. Transactions of the AIME 146, 54–62.

Avdeev, D.B., 2005. Three-dimensional electromagnetic modelling and inversion from theory to application. Surveys in Geophysics 26, 767–799.

Bælum, K., Braathen, A., 2012. Along-strike changes in fault array and rift basin geometry of the Carboniferous Billefjorden Trough, Svalbard, Norway. Tectonophysics 546, 38–55.

Bahr, K., 1988. Interpretadon of the magnetotelluric impedance tensor: regional induction and local telluric distortion. Journal of Geophysics 62, 119–127.

Bahr, K., 1991. Geological noise in magnetotelluric data: a classification of distortion types. Physics of the Earth and Planetary Interiors 66, 24–38.

Banks, D., Sletten, R.S., Haldorsen, S., Dale, B., Heim, M., Swensen, B., 1998. The thermal springs of Bockfjord, Svalbard: occurrence and major ion hydrochemistry. Geothermics 27, 445–467.

Berdichevsky, M., 1960. Principles of magnetotelluric profiling theory. Appl. Geophys 28, 70–91.

Berdichevsky, M.N., Dmitriev, V.I., 1976. Basic principles of interpretation of magnetotelluric sounding curves. Geoelectric and geothermal studies , 165–221.

Bergh, S.G., Braathen, A., Andresen, A., 1997. Interaction of basement-involved and thin-skinned tectonism in the Tertiary fold-thrust belt of central Spitsbergen, Svalbard. The American Association of Petroleum Geologists Bulletin 81, 637–661.

Bergh, S.G., Grogan, P., 2003. Tertiary structure of the Sorkapp-Hornsund region, south Spitsbergen, and implications for the offshore southern extension of the fold-thrust belt. Norwegian Journal of Geology 83, 43–60.

Booker, J.R., 2014. The magnetotelluric phase tensor: a critical review. Surveys in Geophysics 35, 7–40.

Cagniard, L., 1953. Basic theory of the magnetotelluric method of geophysical prospecting. Geophysics 18, 605–635.

Caldwell, T.G., Bibby, H.M., Brown, C., 2004. The magnetotelluric phase tensor. Geophysical Journal International 158, 457–469.

Chave, A.D., Jones, A.G., 2012. The magnetotelluric method: Theory and practice. Cambridge University Press.

Chave, A.D., Thomson, D.J., Ander, M.E., 1987. On the robust estimation of power spectra, coherences, and transfer functions. J. geophys. Res 92, 633–648.

Cherevatova, M., Smirnov, M.Y., Jones, A., Pedersen, L., Group, M.W., et al., 2015. Magnetotelluric array data analysis from north-west Fennoscandia. Tectonophysics 653, 1–19.

Constable, S.C., Parker, R.L., Constable, C.G., 1987. Occam's inversion: A practical algorithm for generating smooth models from electromagnetic sounding data. Geophysics 52, 289–300.

Dallmann, W.K., 1999. Lithostratigraphic lexicon of Svalbard. Norwegian Polar Institute, Tromsø, p. 318.

Dallmann, W.K., 2007. Geology of svalbard. Geology of the land and sea areas of northern Europe. Norges Geologiske Undersøkelse Special Publication 10, 87–89.

Dallmann, W.K., Ohta, Y., Elvevold, S., Blomeier, D., 2002. Bedrock map of Svalbard and Jan Mayen. Norwegian Polar Institute, Temakart No. 33.

Didana, Y.L., Thiel, S., Heinson, G., 2014. Magnetotelluric imaging of upper crustal partial melt at tendaho graben in afar, ethiopia. Geophysical Research Letters 41, 3089–3095.

Duba, A., Heikamp, S., Meurer, W., Nover, G., Will, G., et al., 1994. Evidence from borehole samples for the role of accessory minerals in lower-crustal conductivity. Nature 367, 59–61.

Egbert, G.D., Booker, J.R., 1986. Robust estimation of geomagnetic transfer functions. Geophysical Journal International 87, 173–194.

Egbert, G.D., Kelbert, A., 2012. Computational recipes for electromagnetic inverse problems. Geophysical Journal International 189, 251–267.

Eiken, O., 1994. Seismic Atlas of Western Svalbard. Norwegian Polar Institute, Meddelelser NR. 130.

Elvebakk, H., 2010. Results of borehole logging in well LYB CO2, Dh4 of 2009, Longyearbyen, Svalbard. Technical Report. Geological Survey of Norway Report.

Elvevold, S., Dallmann, W., Blomeier, D., 2007. Geology of Svalbard. Norwegain Polar Institute.

Evans, S., Jones, A.G., Spratt, J., Katsube, J., 2005. Central Baffin electromagnetic experiment (CBEX): Mapping the North American Central Plains (NACP) conductivity anomaly in the Canadian arctic. Physics of the Earth and Planetary Interiors 150, 107–122.

Faleide, J.I., Tsikalas, F., Breivik, A.J., Mjelde, R., Ritzmann, O., Engen, O., Wilson, J., Eldholm, O., 2008. Structure and evolution of the continental margin off Norway and the Barents Sea. Episodes 31, 82.

Gamble, T., Goubau, W.M., Clarke, J., 1979. Magnetotellurics with a remote magnetic reference. Geophysics 44, 53–68.

Haremo, P., Andresen, A., Dypvik, H., Nagy, J., Elverhøi, A., Eikeland, T.A., Johansen, H., 1990. Structural development along the Billefjorden Fault Zone in the area between Kjellströmdalen and Adventdalen/Sassendalen, central Spitsbergen. Polar Research 8, 195–216.

Harland, W.B., 1997. The geology of Svalbard. Geological Society London, Memoir No. 17.

Jakobsson, M., Mayer, L., Coakley, B., Dowdeswell, J.A., Forbes, S., Fridman, B., Hodnesdal, H., Noormets, R., Pedersen, R., Rebesco, M., et al., 2012. The international bathymetric chart of the Arctic Ocean (IBCAO) version 3.0. Geophysical Research Letters 39 (12).

Jiracek, G.R., 1990. Near-surface and topographic distortions in electromagnetic induction. Surveys in Geophysics 11, 163–203.

Jones, A.G., 1999. Imaging the continental upper mantle using electromagnetic methods. Developments in Geotectonics 24, 57–80.

Karato, S., 1990. The role of hydrogen in the electrical conductivity of the upper mantle. Nature 347, 272–273.

Kelbert, A., Meqbel, N., Egbert, G.D., Tandon, K., 2014. ModEM: a modular system for inversion of electromagnetic geophysical data. Computers & Geosciences 66, 40–53.

Khutorskoi, M., Leonov, Y.G., Ermakov, A., Akhmedzyanov, V., 2009. Abnormal heat flow and the trough's nature in the Northern Svalbard plate, in: Doklady Earth Sciences, Springer. pp. 29–35.

Korja, T., 2007. How is the European lithosphere imaged by magnetotellurics? Surveys in Geophysics 28, 239–272.

Ledo, J., Queralt, P., Martí, A., Jones, A.G., 2002. Two-dimensional interpretation of three-dimensional magnetotelluric data: An example of limitations and resolution. Geophysical Journal International 150, 127–139.

Li, S., Unsworth, M.J., Booker, J.R., Wei, W., Tan, H., Jones, A.G., 2003. Partial melt or aqueous fluid in the mid-crust of Southern Tibet? Constraints from INDEPTH magnetotelluric data. Geophysical Journal International 153, 289–304.

Menke, W., 1989. Geophysical data analysis: discrete inverse theory. San Diego: Academic press.

Meqbel, N.M., Egbert, G.D., Wannamaker, P.E., Kelbert, A., Schultz, A., 2014. Deep electrical resistivity structure of the northwestern US derived from 3-D inversion of USArray magnetotelluric data. Earth and Planetary Science Letters 402, 290–304.

Meqbel, N.M.M., 2009. The electrical conductivity structure of the Dead Sea Basin derived from 2D and 3D inversion of magnetotelluric data. Ph.D. thesis. Freie Universität Berlin, Germany.

Mitchell, B., Bungum, H., Chan, W., Mitchell, P., 1990. Seismicity and present-day tectonics of the Svalbard region. Geophysical Journal International 102, 139–149.

Muñoz, G., 2014. Exploring for geothermal resources with electromagnetic methods. Surveys in geophysics 35, 101–122.

Newman, G.A., Alumbaugh, D.L., 2000. Three-dimensional magnetotelluric inversion using non-linear conjugate gradients. Geophysical journal international 140, 410–424.

Palacky, G., 1987. Resistivity characteristics of geologic targets, in Nabighian, M.N., ed.,. Electromagnetic methods in applied geophysics: Tulsa, Okla., Society of Exploration Geophysicists, 1, 53–129.

Parker, R.L., 1994. Geophysical inverse theory. Princeton university press.

Parkinson, W., 1962. The influence of continents and oceans on geomagnetic variations. Geophysical Journal International 6, 441–449.

Pascal, C., Balling, N., Barrere, C., Davidsen, B., Ebbing, J., Elvebakk, H., Mesli, M., Roberts, D., Slagstad, T., Willemoes-Wissing, B., 2011. HeatBar Final Report 2010, Basement Heat Generation and Heat Flow in the western Barents Sea-importance for hydrocarbon systems. Technical Report. Geological Survey of Norway.

Pirli, M., Schweitzer, J., Ottemöller, L., Raeesi, M., Mjelde, R., Atakan, K., Guterch, A., Gibbons, S.J., Paulsen, B., Debski, W., et al., 2010. Preliminary analysis of the 21 February 2008 Svalbard (Norway) seismic sequence. Seismological research letters 81, 63–75.

Rodi, W., Mackie, R.L., 2001. Nonlinear conjugate gradients algorithm for 2-D magnetotelluric inversion. Geophysics 66, 174–187.

Samrock, F., Kuvshinov, A., Bakker, J., Jackson, A., Fisseha, S., 2015. 3-D analysis and interpretation of magnetotelluric data from the Aluto-Langano geothermal field, Ethiopia. Geophysical Journal International 202, 1923–1948.

Shankland, T., Duba, A., Mathez, E., Peach, C., 1997. Increase of electrical conductivity with pressure as an indicator of conduction through a solid phase in midcrustal rocks. Journal of Geophysical Research 102.

Simpson, F., Bahr, K., 2005. Practical magnetotellurics. Cambridge University Press.

Siripunvaraporn, W., Egbert, G., 2000. An efficient data-subspace inversion method for 2-D magnetotelluric data. Geophysics 65, 791–803.

Siripunvaraporn, W., Egbert, G., Lenbury, Y., Uyeshima, M., 2005. Three-dimensional magnetotelluric inversion: data-space method. Physics of the Earth and Planetary Interiors 150, 3–14.

Slagstad, T., Balling, N., Elvebakk, H., Midttømme, K., Olesen, O., Olsen, L., Pascal, C., 2009. Heat-flow measurements in Late Palaeoproterozoic to Permian geological provinces in south and central Norway and a new heat-flow map of Fennoscandia and the Norwegian–Greenland Sea. Tectonophysics 473, 341–361.

Smirnov, M., Korja, T., Dynesius, L., Pedersen, L.B., Laukkanen, E., 2008. Broadband magnetotelluric instruments for near-surface and lithospheric studies of electrical conductivity: a Fennoscandian pool of magnetotelluric instruments. Geophysica 44, 31–44.

Smirnov, M.Y., 2003. Magnetotelluric data processing with a robust statistical procedure having a high breakdown point. Geophysical Journal International 152, 1–7.

Smirnov, M.Y., Pedersen, L.B., 2009. Magnetotelluric measurements across the Sorgenfrei-Tornquist Zone in southern Sweden and Denmark. Geophysical Journal International 176, 443–456.

Spichak, V., Manzella, A., 2009. Electromagnetic sounding of geothermal zones. Journal of Applied Geophysics 68, 459–478.

Steel, R.J., Worsley, D., 1984. Svalbard's post-Caledonian strata-an atlas of sedimentational patterns and palaeogeographic evolution, in: Petroleum geology of the North European margin. Springer, pp. 109–135.

Stegena, L., 1976. Electric conductivity structure and geothermal reservoirs. Acta Geodaet., Geophys. et Montanist. Acad. Sci. Hung. Tomus 11, 377–397.

Streich, R., Becken, M., Ritter, O., 2010. Imaging of CO2 storage sites, geothermal reservoirs, and gas shales using controlled-source magnetotellurics: modeling studies. Chemie Der Erde-Geochemistry 70, 63–75.

Swift, C.M., 1967. A magnetotelluric investigation of an electrical conductivity anomaly in the southwestern United States. Ph.D. thesis. Massachusetts Institute of Technology.

Tikhonov, A., 1950. On determining electrical characteristics of the deep layers of the earth's crust, in: Sov. Math. Dokl, pp. 295–297.

Tikonov, A.N., Arsenin, V.Y., 1977. Solutions of ill-posed problems. New York: Winston .

Treiman, A.H., 2012. Eruption age of the Sverrefjellet volcano, Spitsbergen Island, Norway. Polar Research 31.

Vågnes, E., Amundsen, H.E.F., 1993. Late Cenozoic uplift and volcanism on Spitsbergen: Caused by mantle convection? Geology 21, 251–254.

Vozoff, K., 1972. The magnetotelluric method in the exploration of sedimentary basins. Geophysics 37, 98–141.

Vozoff, K., 1991. The magnetotelluric method, in Electromagnetic methods in applied geophysics. edited by M. N. Nabighian, 02 ed., Soc. Expl. Geophys.

Wannamaker, P.E., 2000. Comment on "The petrologic case for a dry lower crust" by Bruce WD Yardley and John W Valley. Journal of Geophysical Research: Solid Earth 105, 6057–6064.

Wannamaker, P.E., Hohmann, G.W., Ward, S.H., 1984. Magnetotelluric responses of three-dimensional bodies in layered earths. Geophysics 49, 1517–1533.

Waxman, M., Smits, L., et al., 1968. Electrical conductivities in oil-bearing shaly sands. Society of Petroleum Engineers Journal 8, 107–122.

Weaver, J.T., 1994. Mathematical methods for geo-electromagnetic induction. volume 7. Research Studie.

Wiese, H., 1965. Geomagnetische Induktionspfeile in der čssr, Hervorgerufen durch Grossräumige Elektrische Leitfähigkeitsstrukturen. Studia Geophysica et Geodaetica 9, 415–419.

Worsley, D., 2008. The post-Caledonian development of Svalbard and the western Barents Sea. Polar Research 27, 298–317.

Yoshino, T., Manthilake, G., Matsuzaki, T., Katsura, T., 2008. Dry mantle transition zone inferred from the conductivity of wadsleyite and ringwoodite. Nature 451, 326–329.

Yoshino, T., Matsuzaki, T., Yamashita, S., Katsura, T., 2006. Hydrous olivine unable to account for conductivity anomaly at the top of the asthenosphere. Nature 443, 973–976.

Zhang, P., Roberts, R., Pedersen, L., 1987. Magnetotelluric strike rules. Geophysics 52, 267–278.

Zhdanov, M.S., Keller, G.V., 1994. The geoelectrical methods in geophysical exploration. volume 31. Elsevier Science Limited.

Zonge, K.L., Hughes, L.J., 1985. The effect of electrode contact resistance on electric field measurements, in: Expanded Abstracts of 1985 Technical Programme of 55th Ann. Int. SEG Meeting, pp. 231–234.